



**HAL**  
open science

## ARFBF morphological analysis - Application to the discrimination of catalyst active phases

Zhangyun Tan, Maxime Moreaud, Olivier Alata, Abdourrahmane Atto

► **To cite this version:**

Zhangyun Tan, Maxime Moreaud, Olivier Alata, Abdourrahmane Atto. ARFBF morphological analysis - Application to the discrimination of catalyst active phases. *Image Analysis & Stereology*, 2018, 37 (1), pp.21-34. 10.5566/ias.1624 . hal-01779425v1

**HAL Id: hal-01779425**

**<https://hal.science/hal-01779425v1>**

Submitted on 24 Jul 2018 (v1), last revised 29 Jan 2019 (v2)

**HAL** is a multi-disciplinary open access archive for the deposit and dissemination of scientific research documents, whether they are published or not. The documents may come from teaching and research institutions in France or abroad, or from public or private research centers.

L'archive ouverte pluridisciplinaire **HAL**, est destinée au dépôt et à la diffusion de documents scientifiques de niveau recherche, publiés ou non, émanant des établissements d'enseignement et de recherche français ou étrangers, des laboratoires publics ou privés.



Distributed under a Creative Commons Attribution - NonCommercial 4.0 International License

# ARFBF MORPHOLOGICAL IMAGE ANALYSIS - APPLICATION TO THE DISCRIMINATION OF CATALYST ACTIVE PHASES

ZHANGYUN TAN<sup>1</sup>, MAXIME MOREAUD<sup>2,\*</sup>, OLIVIER ALATA<sup>3</sup>, ABDOURRAHMANE M. ATTO<sup>1</sup>

<sup>1</sup>LISTIC, EA 3703, University Savoie Mont Blanc, France

<sup>2</sup>IFP Energies Nouvelles, BP 3, 69360 Solaize, France

<sup>3</sup>Lab. Hubert Curien, CNRS UMR 5516, Jean Monnet University of Saint-Etienne, France

e-mail: \*maxime.moreaud@ifpen.fr

(Submitted)

## ABSTRACT

This paper addresses the characterization of spatial arrangements of fringes in catalysts imaged by High Resolution Transmission Electron Microscopy (HRTEM). It presents a statistical model-based approach for analyzing these fringes. The proposed approach involves Fractional Brownian Field (FBF) and 2-D Auto-Regressive (AR) modeling, as well as morphological analysis. The originality of the approach consists in identifying the image background as an FBF, subtracting this background, modeling the residual by 2-D AR so as to capture fringe information and, finally, discriminating catalysts from fringe characterizations obtained by morphological analysis. The overall analysis is called ARFBF (Auto-Regressive Fractional Brownian Field) based morphology characterization.

Keywords: Texture Analysis, Fractional Brownian Field, Auto-Regressive Field, Mathematical Morphology, HRTEM Imaging..

## INTRODUCTION

Texture analysis plays a key role in almost all imaging systems (radar, sonar, X-ray, microscopy ...) and human visual perception. Texture structure characterization has deserved a considerable amount of works in order to describe image patterns for feature recognition (see (Qazi et al., 2011; Goncalves and Bruno, 2013), among other references).

In recent literature, material texture characterization at nanoscale using image analysis has been considered with either qualitative or quantitative methods. For instance, (Da Costa et al., 2015) investigated carbon planes with orientation description, (Pré et al., 2013) considered activated carbon with mathematical morphology approach, (Moreaud et al., 2012) studied alumina platelets using morphological random model-based approach, (Toth et al., 2013) investigated soot with multi-resolution approach, (Zhang et al., 2011) considered active phases of unsupported hydrodesulphurization catalyst and (Moreaud et al., 2008) investigated ceria active phase using local frequency segmentation approach and morphological analysis.

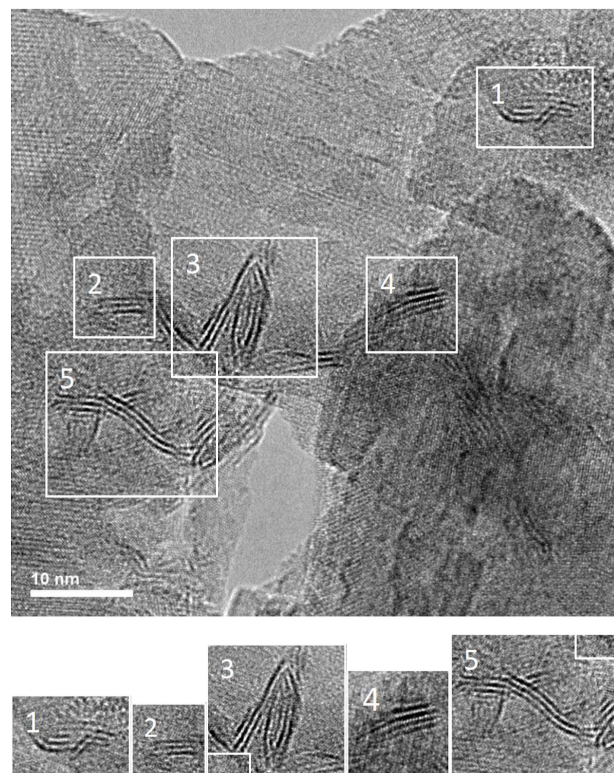


Figure 1. *Molybdenum sulfide sheets (black fringes) deposited on an alumina support (top image) and its sub-images (significant fringes selected, in the second row). The initial image consists of  $1024 \times 1024$  pixels. The numerical resolution is 0.057 nm by pixel.*

In this paper, we are interested in the characterization of hydrotreating catalysts with sulphide phases supported on alumina (see (Toulhoat and Raybaud, 2013), (Celce et al., 2008)) using statistical model-based approach. Samples were observed by high resolution transmission electron microscopy, using a JEOL TEM 2100F operated at 200kV, whose point-to-point resolution is 0.23 nm. The so-called CoMoS<sup>1</sup> active phase consists of nanolayers of MoS<sub>2</sub>, decorated at the edges with Co atoms. When their basal plane is oriented parallel to the electron beam axis, then they appear as black fringes. They can be either isolated or stacked with a stacking number up to 5 usually. If the catalyst presents a high loading of active phase, nanolayers can also form aggregates filling the support porosity. Length and stacking number of the nanolayers depend on several parameters: nature of the support, impregnation and sulfidation methods. They directly impact the activity and selectivity of the catalyst (see (Toulhoat and Raybaud, 2013) and (Nikulshin et al., 2014)).

Active phases shown in Fig.1 can be seen as pseudo-periodic fields, a property which can be captured by using a 2-D Auto-Regressive model (2-D AR). Indeed, the 2-D AR random field model has shown relevancy for describing a wide class of pseudo-periodic textures (see (Alata and Ramananjara, 2005; Mao and Jain, 1992; Haralick, 1979; Souza, 1982) for the relevancy of this model in classification, segmentation and recognition of textural information). We thus consider the AR model for characterizing the active phases and propose using AR field power spectrum in order to derive their features. The spectrum of 2-D AR model can be calculated by the Harmonic Mean (HM) method (see (Jackson and Chien, 1979; Alata et al., 1998)).

The nanolayers are deposited on a crystalline alumina support (Fig.1). Observations at high resolution also produce fringes (corresponding to atomic planes) and Moire fringes. Nevertheless, their contrast and their periodicity differ from those of CoMoS nanolayers, preventing confusion. Moreover, post-treated areas correspond to the thinnest zones of the sample, where alumina contribution is minored. This background is considered here as a noisy field interacting with the intrinsic AR model and it has to be removed or attenuated significantly so as to make AR modeling efficient. For this purpose, we propose using a 2-D Fractional Brownian Field (FBF) for

modeling this undesirable interaction, prior to AR modeling.

FBF is the spatial extension of the fractional Brownian motion (fBm), a non-stationary process derived by (Mandelbrot and Ness, 1968). Several variants of FBF exist, among which the separable and isotropic extensions. We consider hereafter the isotropic FBF whose characterizations are given in (Pesquet-Popescu and Véhel, 2002; Huang and Li, 2005; Pesquet-Popescu and Larzabal, 1997; Richard and Bierme, 2010; Atto et al., 2014). Isotropic FBF is a one-parameter model. Its parameter, called *Hurst parameter*, is representative of stochastic regularity (texture roughness, in practice). In this respect, it suits for the description of the heterogeneous HRTEM image background.

In the literature, several methods exist for estimating the Hurst parameter of the 2-D FBF, for instance, maximum likelihood estimates (see (Tafti et al., 2009; Fieguth and Willsky, 1996)), box-counting approach (see (Huang et al., 1994)) and log-periodogram methods (see (Geweke and Porter-Hudak, 1983; Robinson, 1995)). Because FBF admits one pole located at zero frequency in the spectral domain (infinite spectral value at zero), these estimators lack robustness on small sample sizes. In order to obtain a robust Hurst parameter estimator, we consider the extension to FBF (see (Tan et al., 2015)) of the wavelet packet method of (Atto et al., 2010) dedicated to fractional Brownian motion Hurst parameter estimation. This extension, based on 2-D wavelet packet spectrum, is called *Log-Regression on Polar representation of Wavelet Packet spectrum* (Log-RPWP).

In this paper, we propose an ARFBF based morphology analysis so as to capture HRTEM fringe information. This method relies on:

1. the integration of 2-D FBF and 2-D AR by using a convolution operator in order to define HRTEM ARFBF (Auto-Regressive Fractional Brownian Field, see (Tan et al., 2015)) features and
2. morphological analysis on the basis of the HRTEM ARFBF features.

Summarizing, the originality of the approach consists in identifying the image background as an FBF, subtracting this background, modeling the residual by a 2-D AR which is able to characterize the pseudo-periodic structure of the

<sup>1</sup>CoMoS refers to catalysts consisting of nanolayers of MoS<sub>2</sub>, decorated at the edges with Co atoms.

active phase deposited on the support of catalyst. The contributions presented in this work involve:

- assessing, in comparison with the state of the art (see (Tafti et al., 2009; Van De Ville et al., 2005)), the performance of Log-RPWP Hurst parameter estimation method introduced in (Tan et al., 2015) on different FBF generators,
- deriving an analysis framework by integrating morphological analysis of the ARFBF description,
- addressing HRTEM micrograph morphological texture characterization by using this ARFBF morphological framework,
- discriminating different catalysts from obtained characterizations. A comparison is proposed with a Fourier-based spectrum analysis in order to show the interest of using model-based HM method.

In the next section, we present the 2-D ARFBF model after some recalls about 2-D AR model and FBF model, and after the new results about Hurst parameter estimation. In section 3, 2-D ARFBF morphological analysis of HRTEM is detailed and experimental results about catalyst discrimination are provided. In section 4, the conclusion of this study is provided with some perspectives.

## ARFBF MODEL

The 2-D ARFBF introduced in (Tan et al., 2015) is defined as the convolution with respect to deterministic spatial variables, of AR field  $A$  and isotropic FBF  $B_H$ . This 2-D ARFBF, hereafter denoted  $Z(x, y)$ , is defined as follows,

$$Z(x, y) = (A * B_H)(x, y). \quad (1)$$

Particularly,  $Z$  behaves as an FBF when AR is a white noise;  $Z$  is an AR when FBF is a white noise ( $H = 0$ ).

When an image is associated to an ARFBF observation  $Z$ , this means that the image content can be seen as an AR based filtering of a fractional Brownian texture. The model applies on spatial texture level by describing the spatial covariance structure, in contrast with pixel level models such as marked point processes.

The following Section 2.1 presents the 2-D AR framework used in the paper. Then, Section 2.2 presents the isotropic FBF, as well as an estimation procedure for the parameter of this

model, in addition with a performance validation stage (main contribution of the Section) through a comparison with respect to the state of the art.

## 2-D AR MODEL

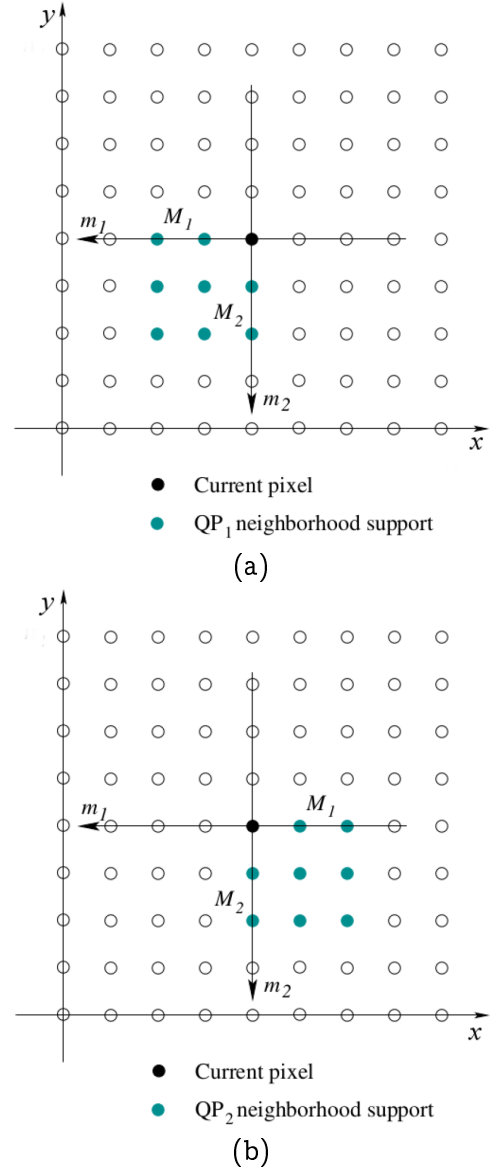


Figure 2. Quarter plan prediction supports denoted (a)  $D_{QP_1}$  (see Eq.(3)) and (b)  $D_{QP_2}$  (see Eq.(4)) with finite order  $(M_1, M_2) = (2, 2)$  and  $(x, y) \in Z^2$ .

Let us define a centered second-order stationary field as  $A = \{A(x, y)\}, (x, y) \in Z^2$ .  $A$  is a 2-D AR process if

$$A(x, y) = - \sum_{m \in D} \beta_m A(x - m_1, y - m_2) + E(x, y), \quad (2)$$

where  $D$  is the prediction support,  $m = (m_1, m_2) \in D$ ,  $E(x, y)$  is an independent and identically

distributed process with zero mean and variance  $\sigma_e^2$ ,  $\beta_m$  are 2-D transverse coefficients.

Different prediction supports can be defined (Alata and Olivier, 2003). In this paper, we will use two prediction supports with Quarter Plan (QP) forms respectively denoted  $QP_\ell$ ,  $\ell = 1, 2$  (Fig.2 shows an illustrative example of these QPs), with:

$$D_{QP_1} = \{0 \leq m_1 \leq M_1, 0 \leq m_2 \leq M_2\} \setminus (0, 0), \quad (3)$$

and

$$D_{QP_2} = \{-M_1 \leq m_1 \leq 0, 0 \leq m_2 \leq M_2\} \setminus (0, 0). \quad (4)$$

$(M_1, M_2)$  is the 2-D AR order. Let us denote the set of AR parameters associated with  $QP_\ell$ ,  $\ell \in \{1, 2\}$ , as

$$\theta_{M_1, M_2}^{QP_\ell} = \{\sigma_{e, \ell}^2, \{\beta_{m, \ell}, m \in D_{QP_\ell}\}\}. \quad (5)$$

At a fixed order, the parameters of  $\theta_{M_1, M_2}^{QP_\ell}$ ,  $\ell \in \{1, 2\}$ , are estimated thanks to minimization in the least-squares sense of prediction errors, see (Ranganath and Jain, 1985; Alata and Cariou, 2008a). This procedure involves Yule-Walker equations and it is equivalent to the maximum likelihood estimation, when the random variables are Gaussian.

In practice, the selection of an accurate prediction support determines model performance. Although a number of works focus on the order  $(M_1, M_2)$  selection, see references (Alata and Olivier, 2003; Akaike, 1974) among others, this paper considers, from preliminary experimental model validation,  $M_1 = M_2 = 10$  as the order of the prediction support.

The 2-D AR Power Spectral Density (PSD),  $S_{AR}(\mathbf{u}, \mathbf{v})$ , is then derived as the harmonic mean of the two spectra associated with prediction supports  $QP_\ell$ ,  $\ell = 1, 2$ , (Jackson and Chien, 1979):

$$S_{AR}(\mathbf{u}, \mathbf{v}) = \frac{2S_{QP_1}(\mathbf{u}, \mathbf{v})S_{QP_2}(\mathbf{u}, \mathbf{v})}{S_{QP_1}(\mathbf{u}, \mathbf{v}) + S_{QP_2}(\mathbf{u}, \mathbf{v})}, \quad (6)$$

where

$$S_{QP_\ell}(\mathbf{u}, \mathbf{v}) = \frac{\sigma_{e, \ell}^2}{|F_{QP_\ell}(\mathbf{u}, \mathbf{v})|^2} \quad (7)$$

and

$$F_{QP_\ell}(\mathbf{u}, \mathbf{v}) = 1 + \sum_{m=(m_1, m_2) \in D_{QP_\ell}} \beta_{m, \ell} e^{-i2\pi m_1 u} e^{-i2\pi m_2 v}.$$

The 2-D spectrum estimated from this method is easy to compute and has good estimation properties with respect to the other existing methods, see (Alata and Cariou, 2008b) for details.

## 2-D FBF ISOTROPIC MODEL AND HURST PARAMETER ESTIMATION

### 2-D FBF model

The 2-D isotropic FBF with Hurst parameter  $H$ ,  $0 < H < 1$ , denoted here as  $B_H(x, y)$ , is defined to be a non-stationary Gaussian zero-mean real-valued field with auto-correlation function defined as

$$R_{B_H}(t, s) = \frac{\sigma_b^2}{2} (\|t\|^{2H} + \|s\|^{2H} - \|t-s\|^{2H}) \quad (8)$$

where  $\sigma_b^2$  is a constant representing the variance of a white Gaussian noise.

Although FBF is a non-stationary process, this random process has stationary-increments and stationary wavelet projections. The spectrum of FBF can then be defined by association with respect to the above stationary FBF instances and is given by (see (Pesquet-Popescu and V  hel, 2002; Huang and Li, 2005; Richard and Bierme, 2010; Atto et al., 2014)):

$$\begin{aligned} S_{FBF}(\mathbf{u}, \mathbf{v}) &= \xi(H) \frac{1}{(u^2 + v^2)^{H+1}} \\ &= \xi(H) \frac{1}{\|(\mathbf{u}, \mathbf{v})\|^{2H+2}}, \end{aligned} \quad (9)$$

where  $\|(\mathbf{u}, \mathbf{v})\| = \sqrt{u^2 + v^2}$ ,

$$\xi(H) = \frac{2^{-(2H+1)} \pi^2 \sigma_b^2}{\sin(\pi H) \Gamma^2(1+H)}$$

and  $\Gamma$  is the standard gamma function.

Sample FBF		Log-RPWP		Log-RPHW		ML-PHW	
	H	$\hat{H}$	std	$\hat{H}$	std	$\hat{H}$	std
Generator #1	0.2	0.210	0.031	0.204	0.009	0.200	0.006
	0.4	0.427	0.020	0.392	0.012	0.392	0.009
	0.6	0.643	0.039	0.600	0.010	0.597	0.007
	0.8	0.877	0.017	0.792	0.006	0.793	0.004
Generator #2	0.2	0.156	0.018	-0.029	0.004	-0.088	0.005
	0.4	0.424	0.026	0.264	0.014	0.226	0.010
	0.6	0.579	0.033	0.452	0.024	0.362	0.035
	0.8	0.815	0.048	0.415	0.029	0.313	0.023

Table 1. Mean values and standard deviations for estimated Hurst parameters from Monte-Carlo simulations with 10 FBF realizations.

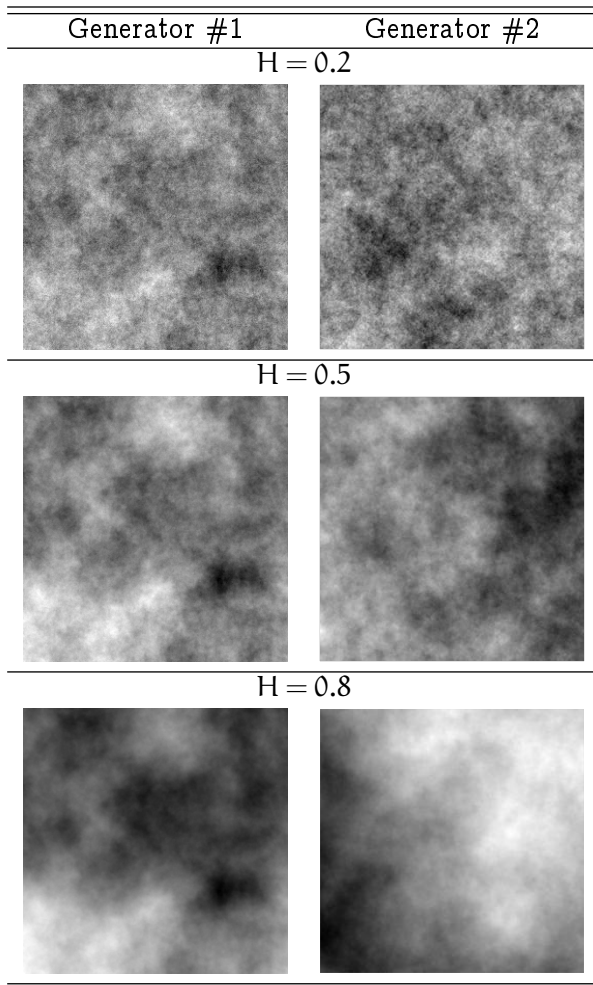


Figure 3. Examples of sample FBFs used for Monte-Carlo simulations in Table 1.

For Hurst parameter estimation, we propose the Log-RPWP method introduced in (Tan et al., 2015). Log-RPWP Hurst parameter estimation method consists of three steps.

- In the first step, the spectrum with polar coordinates  $S_p$  is computed as,

$$S_p(r, \theta) = T(\hat{S}_{\text{FBF}}(u, v)), \quad (10)$$

where  $\hat{S}_{\text{FBF}}(u, v)$  is the wavelet packet spectrum ((Atto et al., 2013)), in Cartesian coordinates  $(u, v)$ , estimated from FBF samples and  $T$  is the Cartesian-to-polar transform.

- In the second step, averages are done over the angles:

$$S_p(r_i) = \frac{1}{J} \sum_{j=1}^J S_p(r_i, \theta_j), \quad (11)$$

with  $1 \leq i \leq N$  denoting the radial sampling index.

- In the third step,  $H$  is estimated by:

$$\hat{H}_{\text{RPWP}} = \frac{1}{2C} \sum_{\substack{1 \leq i, k \leq N \\ i < k}} \frac{\log S_p(r_i) - \log S_p(r_k)}{\log r_k - \log r_i} - 1 \quad (12)$$

where  $C = \frac{N!}{2(N-2)!}$  is the number of all possible combinations of indices  $(i, k)$  such that  $0 < i < k \leq N$ .

Performance assessment of Log-RPWP Hurst parameter estimator

In this section, we compare the 2-D Log-RPWP Hurst parameter estimation method to two standard estimators: the first estimator performs Log-Regression based on Poly-Harmonic Wavelets (denoted hereafter as Log-RPHW) and the second estimator performs Maximum Likelihood (ML-PHW) on Poly-Harmonic Wavelets, both estimators being proposed in (Tafti et al., 2009).

The experimental setup concerns FBF sampling from random number generators. Two generators are used for experimental tests: the Generator #1 of (Van De Ville et al., 2005) is an FBF synthesis *via* projections on PolyHarmonic wavelets and the Generator #2 proposed by (Kroese and Botev, 2013) is a direct spatial

synthesis by imposing the covariance structure of Eq. (8).

Tab.1 gives, for FBF Generators #1 and #2 (see sample FBFs given by Fig.3), the best relevant Hurst parameter estimations for all Log-RPWP, Log-RPHW and ML-PHW, when the maximal wavelet decomposition level is limited to 7 (sample realizations are with sizes  $512 \times 512$ ). Hurst parameter estimation was realized from Monte-Carlo simulations on 10 FBF realizations and  $H \in \{0.2, 0.4, 0.6, 0.8\}$ .

One can observe from Tab.1 that accuracy of Log-RPHW and ML-PHW methods are limited to the Polyharmonic FBF: this is due to that the latter is synthesized by using the same wavelets as those involved in Log-RPHW and ML-PHW estimation routines. However, Log-RPHW and ML-PHW methods fail to estimate Hurst parameter of Generator #2's FBF, which uses no *a priori* on a specific wavelet generating function.

In contrast to Log-RPHW and ML-PHW, the Log-RPWP method gives relevant results whatever the generator used to derive FBF samples, as it can be seen in Tab.1. In the following experimental tests on real word data, we thus focus on Log-RPWP estimator which guarantees robustness of the Hurst parameter estimation.

## ARFBF MODELING PROCEDURE FOR HRTEM IMAGE

From Eq.(1), the spectrum associated with the non-stationary ARFBF model is

$$S_{\text{ARFBF}}(\mathbf{u}, \mathbf{v}) = S_{\text{AR}}(\mathbf{u}, \mathbf{v}) S_{\text{FBF}}(\mathbf{u}, \mathbf{v})$$

and reduces to (Eq. (6) & (9)):

$$S_{\text{ARFBF}}(\mathbf{u}, \mathbf{v}) = \frac{2S_{\text{QP}_1}(\mathbf{u}, \mathbf{v})S_{\text{QP}_2}(\mathbf{u}, \mathbf{v})}{S_{\text{QP}_1}(\mathbf{u}, \mathbf{v}) + S_{\text{QP}_2}(\mathbf{u}, \mathbf{v})} \frac{\xi(H)}{\|(\mathbf{u}, \mathbf{v})\|^{2H+2}}, \quad (13)$$

where  $S_{\text{QP}_1}$  and  $S_{\text{QP}_2}$  are defined by Eq.(7).

From Eq.(13), the spectrum of ARFBF has one singular frequency at the zero frequency point. Let us denote one HRTEM image as  $I$ . The modeling procedure of the of  $I$  by using an ARFBF involves the following spectral processing:

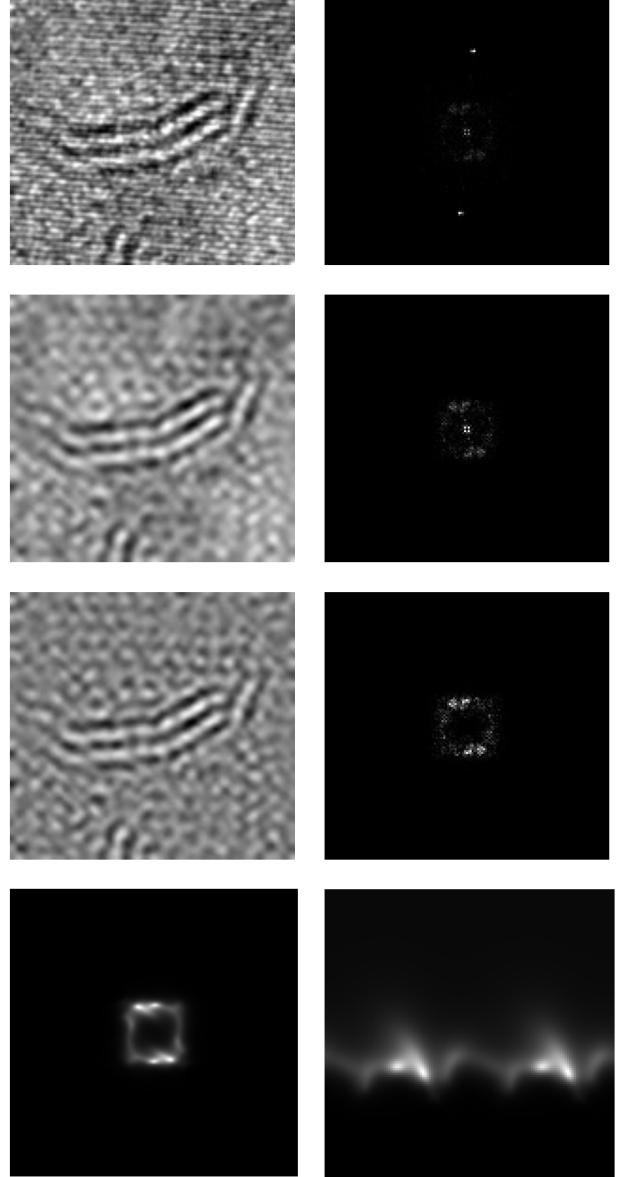


Figure 4. ARFBF modeling of HRTEM image. In the first row, the original image  $I_1$  and its PSD  $S_1$ ; in the second row, the image  $I_2$  (after WHFR pre-processing) and its PSD  $S_2$ ; in the third row, the image  $I_3$  (after removing the FBF contribution from the image  $I_2$ ) and its PSD  $S_3$ . Finally, the last row presents the PSD calculated with the parameters estimated by AR modeling in Cartesian coordinate (left) and in polar coordinate (right - lines are associated with radii and columns to angles).

- First step, calculate the spectrum  $S_I$  of  $I$  from the periodogram or by using the wavelet packet method of (Atto et al., 2013);
- Second step, estimate, by using the Log-RPWP method presented in Section 2.1, the parameter

$H$  from  $S_I$  and thus  $S_{\text{FBF}}$  is derived.

- Third step, remove the contribution of the FBF in  $I$ . The spectrum of the residual part is denoted as:

$$S_{\text{residual}}(u, v) = \frac{S_I(u, v)}{S_{\text{FBF}}(u, v)}.$$

- Final step, model the residual part by the 2-D AR and calculate its PSD  $S_{\text{AR}}$  from the AR estimated parameters ( $S_{\text{AR}}$  is a smoothed version of  $S_{\text{residual}}$  in general).

## MORPHOLOGY BASED ARFBF ANALYSIS AND APPLICATION TO HRTEM

### ARFBF MODELING OF HRTEM IMAGE

Fig.4 shows an HRTEM image of fringes (Row 1 - Left). Such an image shows high frequency disturbances (thin and almost horizontal lines) induced by the alumina support of the catalyst and a pre-processing step is required in order to remove these disturbances. Once the pre-processing is performed<sup>2</sup>, we obtain in the second row of Fig.4, a pre-processed HRTEM image  $I_2$  which is free of very high frequencies (Row 2- Left). We then remove the FBF contribution from the image  $I_2$  and derive the image  $I_3$  shown in 'Row 3 - Left' of Fig.4. Fig.4 also shows, in the second (right) column, the spectral information<sup>3</sup>  $S_1, S_2, S_3$  associated with images  $I_1, I_2, I_3$  respectively.

Finally, we estimate from  $I_3$  the AR parameters associated to the two QPs (see Section 2.1) and derive the corresponding spectral information. In the last row of Fig.4, the 2-D AR PSD (see Eq. 6) is shown in Cartesian coordinates ( $S^*(u, v)$ , Row 4 - Left, origin at the center) and in polar coordinates ( $S^*(r, \theta)$ , Row 4 - Right, origin at the top left). These are the spectral fringe features derived from ARFBF analysis. When considering a large amount of HRTEM images, we observe that any spectrum  $S^*(u, v), S^*(r, \theta)$  can contain one or several main bump(s) whose forms are associated to the active phase inside the HRTEM image.

One can notice that spectra  $S_1$  and  $S_2$  both contain a peak at the center (zero frequency)

whereas this peak has been removed (it is not related to the active phase we wish to model) in spectrum  $S_3$ , due to FBF subtraction. Moreover, the consequence of FBF subtraction enhances fringe spectral features (ring around the center of the spectrum). This justifies the combination of AR and FBF models proposed in this paper.

We now address in the next section, morphological analysis of the bumps (lobes) involved in the fringe spectral rings.

### MORPHOLOGICAL ANALYSIS OF HRTEM IMAGE

The nanolayer morphology, size and organization on the support of active phases can be observed directly by HRTEM imaging. The analysis of these fringes is generally composed of several steps: noise reduction, contrast enhancement, segmentation and morphological analysis such as length and tortuosity measurements (see (Yehliu et al., 2011)). We propose hereafter a completely different approach with characterization in the frequency domain to obtain information about regularity of spacing or regularity of curvature of layers of fringes. Another advantage of the frequency domain is to separate the information associated with "superimposed" fringes with different main orientations which produces different bumps. However, analysis in this domain is an intricate work because of high frequency disturbances due to acquisition noise, and low frequency disturbances due to the effect of the catalyst support in HRTEM image acquisition. Our approach uses wavelet filtering, suppression of catalyst support contribution by means of an FBF modeling, and an AR model to smooth the residue image corresponding to fringe information. The processed spectral images (see last row of of Fig.4 for instance) show some lobes corresponding to the fringes. A morphological characterization of these lobes will allows us to: 1) obtain information about inter fringe distance and regularity of fringe spacing, (2) observe fringe distance variations and regularity of a fringe curvature by looking at the tangential length of the lobe characterizing the fringe under consideration.

In the following, we propose a morphological analysis of these lobes which are present in the polar representation of the PSD calculated from

<sup>2</sup>We consider Wavelet based High Frequency Removal, WHFR, by forcing wavelet details to zero and reconstructing an image from wavelet approximations, see (Nason and Silverman, 1995).

<sup>3</sup>PSD estimated using periodogram which is based on the square modulus of discrete Fourier transform. The origin is at the center of the images which exhibit central symmetry.



AR estimated parameters (image  $S^*(r, \theta)$  in Fig.4). First, we search the point  $P_1[r^*, \theta^*]$  denoting maximum value of  $S^*$  and we calculate an adaptive threshold  $\alpha_1$  as follows:

$$P_1 = \operatorname{argmax}_{r, \theta} S^*(r, \theta), \quad (14)$$

and

$$\alpha_1 = \lambda_1 S^*(P_1), \quad (15)$$

with  $\lambda_1 \in [0; 1]$ .

In our application, we chose  $\lambda_1 = 0.8$  after validation tests. Segmentation with  $\alpha_1$  can lead to several connected components. This issue can be easily handled by using a morphological reconstruction (see (Serra, 1988)) with  $P_1$  as a marker. A first lobe is obtained on a binary image  $Q_1$ :

$$Q_1 = \gamma_{\text{rec}}^{S^{**}}(P_1), \quad (16)$$

and

$$S^{**}(r, \theta) = \begin{cases} 1, & \text{if } S^*(r, \theta) > \alpha_1, \\ 0, & \text{otherwise.} \end{cases} \quad (17)$$

If a second lobe is located on  $S^*$ , it can be obtained using a similar procedure. The contribution of the first lobe is removed on  $S^*$  using morphological dilation with a disc of radius  $R$  on  $Q_1$ :

$$S_1^*(r, \theta) = \begin{cases} S^*(r, \theta), & \text{if } \delta_R(Q_1) \neq 0, \\ 0, & \text{otherwise.} \end{cases} \quad (18)$$

From available HRTEM data (see samples given in Fig.1 for illustration),  $R = 2$  is efficient. Then a new threshold  $\alpha_2$  is calculated and a binary image  $Q_2$  is obtained by:

$$\alpha_2 = \lambda_2 S^*(P_1), \quad (19)$$

with  $\lambda_2 \in [0; \lambda_1]$ ,

$$P_2 = \operatorname{argmax}_{r, \theta} S_1^*(r, \theta), \quad (20)$$

$$Q_2 = \gamma_{\text{rec}}^{S_1^{**}}(P_2), \quad (21)$$

and

$$S_1^{**}(r, \theta) = \begin{cases} 1, & \text{if } S_1^*(r, \theta) > \alpha_2, \\ 0, & \text{otherwise.} \end{cases} \quad (22)$$

In our application, we chose  $\lambda_2 = 0.6$  (selection from validation tests). In contrast with  $Q_1$ ,  $Q_2$  value is not necessarily non-zero (if there is no remaining significant second lobe). We limit the study to the detection of two lobes in this

experimental setup, with the knowledge that observation of more than two layers of overlapping fringes is rare in our application.

For each lobe on images  $Q_i$ ,  $i = 1$  or  $2$ , denoting a layer of fringes, an average spatial distance between atomic layers is estimated by the distance value  $G$ ,

$$G = \frac{T_e}{r^*}, \quad (23)$$

associated to the maximum of the lobe  $P_i = [r^*, \theta^*]$ ,  $i = 1$  or  $2$ ,  $T_e$  is the sampling period (here,  $T_e = 0.057$ ).

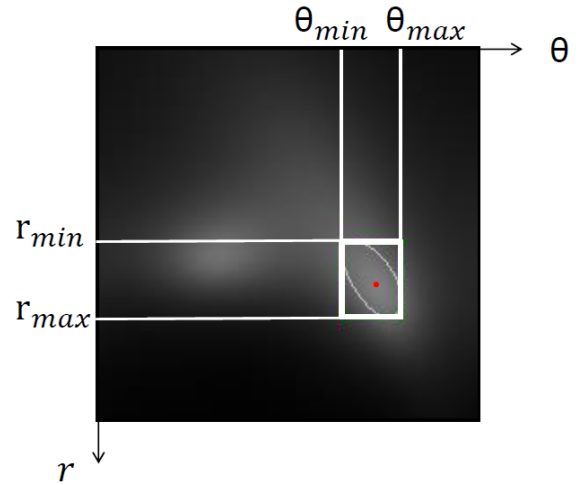


Figure 5. The spectral lobe detected can be considered as an ellipse embedded in a bounding box  $(r_{\min}, r_{\max}, \theta_{\min}, \theta_{\max})$ .

Lobe on binary image  $Q_i$ ,  $i = 1$  or  $2$ , can be considered as an ellipse embedded in a bounding box  $(r_{\min}, r_{\max}, \theta_{\min}, \theta_{\max})$  (see Fig.5). The extension of the lobe allows us to describe the changes in the distance between atomic layers (regularity of spacing) and in the curvature of atomic layers (regularity of curvature). The regularity of spacing and regularity of curvature can be estimated by distance variation  $\Delta_G$  (see Eq.(24)) and tangential length  $L_\theta$  (see Eq.(27)) respectively.  $\Delta_G$  and  $L_\theta$  are defined by:

$$\Delta_G = |G_{\max} - G_{\min}| \quad (24)$$

with

$$G_{\max} = \frac{T_e}{r_{\min}} \quad (25)$$

$$G_{\min} = \frac{T_e}{r_{\max}} \quad (26)$$

where  $T_e = 0.057$ , and

$$L_\theta = |\theta_{\max} - \theta_{\min}|. \quad (27)$$

In the next section, we present our statistical analysis for the discrimination of catalyst active phases.

## STATISTICAL ANALYSIS FOR CATALYST DISCRIMINATION

Based on the geometric features described previously, a comparison between two catalysts is presented. The point-to-point resolution of the TEM is 0.23 nm. The pixel size of the images is 0.057 nm, at an image resolution of  $1024 \times 1024$ . For catalyst 1 (Cat<sub>1</sub>), 78 sub-images containing active phases are taken from 21 HRTEM images. For catalyst 2 (Cat<sub>2</sub>), 88 sub-images containing active phases are taken from 19 HRTEM images. For each sample, we calculate geometric features  $G$ ,  $\Delta_G$  and  $L_\theta$  on detected lobes.

Cat 1 is a CoMoS catalyst supported on alumina. It presents a high loading of active phase, corresponding to a Mo density of 7 at/nm<sup>2</sup>. Cat 2 is a CoMoS catalyst supported on silica. It presents a low loading of active phase, with a Mo density of 1 at/nm<sup>2</sup>. The mean length and stacking of slabs were measured by HRTEM on a minimum of 200 slabs, using an in-house image processing application (Celse et al., 2008): the image is pre-processed in order to stretch contrast, then a region growing algorithm and active contour techniques are used to obtain slab contours. Cat1 presents a mean slab length of 3.89 nm and a mean stacking number of 2.73; Cat 2 presents a mean slab length of 2.49 nm and a mean stacking number of 2.09.

Statistical distributions of  $G$ ,  $\Delta_G$  and  $L_\theta$

The distributions of the features are studied by using a Kernel smoothing function  $f_w$  which is defined as follows ((Rosenblatt, 1956; Parzen, 1962)):

$$f_w(x) = \frac{1}{nw} \sum_{i=1}^n K\left(\frac{x-x_i}{w}\right), \quad (28)$$

where  $n$  is the sample size,  $\{x_i\}_{i=1, \dots, n}$  are the set of considered samples,  $x \in \mathbb{R}$ ,  $K(\cdot)$  is the kernel smoothing function and  $w$  is the bandwidth.

Tab.2 gives certain statistic information of distance  $G$  (measured in nm), distance variation  $\Delta_G$  (measured in nm) and tangential lengths  $L_\theta$  (measured in degree) in terms of means,

variances, third and fourth standardized moments (known as skewness and kurtosis) of the detected lobes on Cat<sub>1</sub> and Cat<sub>2</sub> images. Catalyst ( $n$ ) represents the number of samples in Cat<sub>1</sub> and Cat<sub>2</sub> respectively.

For these catalysts, the inter-distance between two neighboring white/black fringes  $G$  is known to be close to 0.615 nm (see (Geantet and Sorbier, 2012)). In Tab.2,  $G$  has almost same value for Cat<sub>1</sub> and Cat<sub>2</sub> (0.611 nm vs 0.593 nm), it confirms  $G$  as a physical characterization. For  $\Delta_G$  and  $L_\theta$  of Cat<sub>1</sub> and  $L_\theta$  of Cat<sub>2</sub>, the positive skewness values in Tab.2 indicates that the tail on the right side is longer or fatter than that of the left side. When the skewness values are bigger, this phenomenon will be clearer (see Fig.6). In contrast, for the other cases, the tail on the left side is longer or fatter than that of the right side (see Fig.6) because of negative skewness values. The kurtosis measures provided "tailedness" information of the distribution of variables  $G$ ,  $\Delta_G$  or  $L_\theta$ . All kurtosis being larger than 3, one can conclude that  $G$  (for both of Cat<sub>1</sub> and Cat<sub>2</sub>) and  $\Delta_G$  (just for Cat<sub>1</sub>) distributions are far from being Gaussian. In addition, when kurtosis are large, this implies that several outliers can be present in the corresponding variables. These observations are confirmed by Fig.6 which shows the statistical distributions of  $G$ ,  $\Delta_G$  or  $L_\theta$  for both catalysts.

### Kolmogorov-Smirnov test for catalyst discrimination

In this section, we propose Kolmogorov-Smirnov (KS) test for comparing Cat<sub>1</sub> and Cat<sub>2</sub> ARFBF morphology characterizations. The KS measure is given by (see (Peacock, 1983) for details)

$$\mathcal{K} = \max_x (|\hat{f}_1(x) - \hat{f}_2(x)|), \quad (29)$$

where  $\hat{f}_1, \hat{f}_2$  are the empirical cumulative distribution functions of catalyst datasets indexed by '1' and '2'. Function  $\hat{f}$  is hereafter the kernel distribution for one of the three features:  $G$ ,  $\Delta_G$  and  $L_\theta$ . A threshold, based on asymptotic of  $\mathcal{K}$ , is used to derive a decision between alternative hypotheses: null hypothesis ( $\mathcal{H} = 0$ ) is that the two samples are drawn from the same catalyst or  $\mathcal{H} = 1$  means that the test rejects the null hypothesis at 5% significance level.

First, Tab.4 highlights that Kolmogorov-Smirnov test makes a clear discrimination between the two catalysts effective when considering

Catalyst (n) Stat	Cat <sub>1</sub> (93)			Cat <sub>2</sub> (109)		
	G	$\Delta_G$	$L_\theta$	G	$\Delta_G$	$L_\theta$
Mean	0.62	0.124	12.323	0.598	0.097	9.988
Variance	0.003	0.002	27.682	0.003	0.002	26.653
Skewness	-0.991	1.222	1.116	-1.135	1.721	1.425
Kurtosis	7.21	4.784	4.572	4.434	9.681	5.913

Table 2. Using AR-based method for PSD estimation in polar coordinates (see Fig.4 & 5), statistics of distance (see Eq.(23)), distance variation (see Eq.(24)) and tangential length (see Eq.(27)) features of the detected lobe of catalyst image databases (Cat<sub>1</sub> and Cat<sub>2</sub>).

Catalyst (n) Stat	Cat <sub>1</sub> (93)			Cat <sub>2</sub> (109)		
	G	$\Delta_G$	$L_\theta$	G	$\Delta_G$	$L_\theta$
Mean	0.63	0.067	13.296	0.61	0.056	12.776
Variance	0.002	0.0006	10.982	0.003	0.0005	13.879
Skewness	-0.56	2.155	1.000	-1.254	1.745	0.634
Kurtosis	5.987	9.525	4.036	4.898	8.786	3.636

Table 3. Using interpolated periodogram in polar coordinates (see Fig.7): statistics of distance (see Eq.(23)), distance variation (see Eq.(24)) and tangential length (see Eq.(27)) features of the detected lobe of catalyst image databases (Cat<sub>1</sub> and Cat<sub>2</sub>).

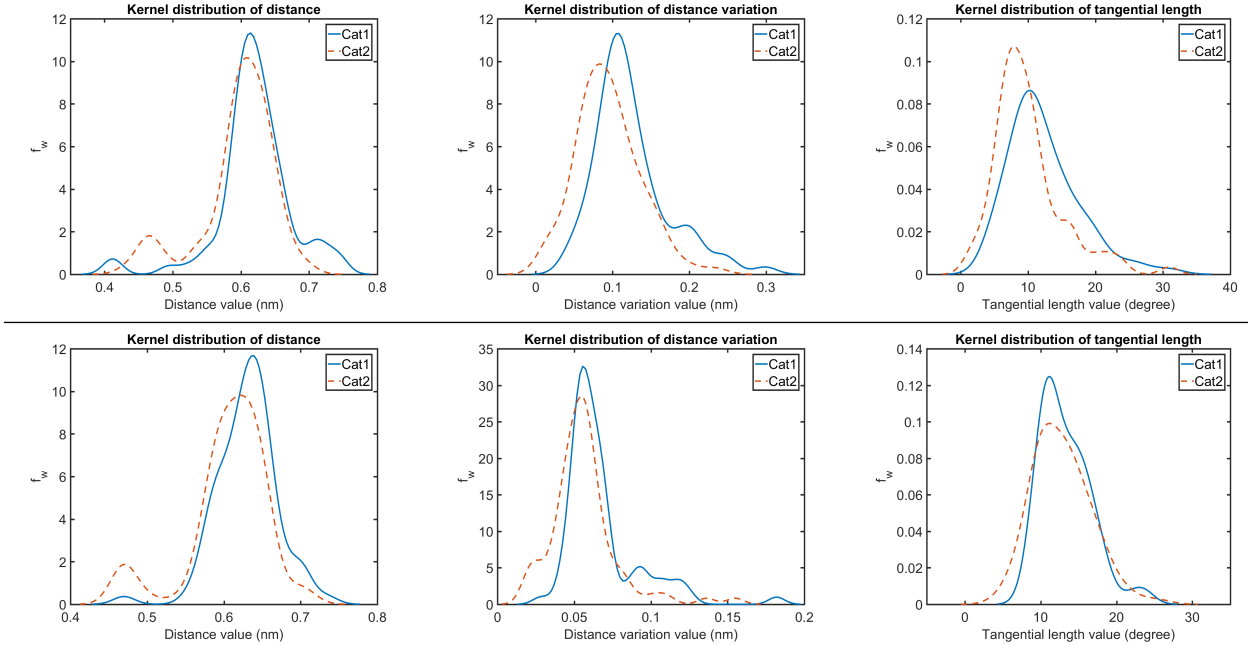


Figure 6. Kernel distributions of distance (left), distance variation (center) and tangential length (right) of the detected lobe  $S_{LobeD}^*$  of Cat<sub>1</sub> (— in blue) and Cat<sub>2</sub> (--- in red). First row: using PSD estimated in polar coordinates with HM method based on the AR model. Second row: Using interpolated periodogram in polar coordinates.

parameters  $\Delta_G$  and  $L_\theta$ . Second, when performing Kolmogorov-Smirnov tests on sub-classes of catalysts Cat<sub>1</sub> and Cat<sub>2</sub> (2 sub-classes per catalyst due to the limited number of available

samples), then the test still performs a relevant discrimination, as it can be seen in Tab.6.

The motivation of using the PSD estimated from an AR model (see Eq. 6 & 13) is also

Statistic	Cat <sub>k</sub> \ Cat <sub>l</sub>	G		$\Delta_G$		$L_\theta$	
		Cat <sub>1</sub>	Cat <sub>2</sub>	Cat <sub>1</sub>	Cat <sub>2</sub>	Cat <sub>1</sub>	Cat <sub>2</sub>
$\mathcal{H}$	Cat <sub>1</sub>	0	0	0	1	0	1
	Cat <sub>2</sub>	0	0	1	0	1	0
$10^3\mathcal{K}$	Cat <sub>1</sub>	0	191	0	316	0	259
	Cat <sub>2</sub>	191	0	316	0	259	0

Table 4. Kolmogorov-Smirnov test for the discrimination of Cat<sub>1</sub> and Cat<sub>2</sub> based on features computed using PSD estimated with AR-based method in polar coordinates. Null hypothesis is rejected at the level  $\alpha = 0.05$  if  $\mathcal{K} > \mathcal{K}_s$  with  $\mathcal{K}_s \approx 1.36\sqrt{\frac{N_1+N_2}{N_1 \times N_2}}$ . With  $N_1 = 78$  (number of samples of Cat<sub>1</sub>) and  $N_2 = 88$  (number of samples of Cat<sub>2</sub>),  $\mathcal{K}_s \approx 0.212$ .

Statistic	Cat <sub>k</sub> \ Cat <sub>l</sub>	G		$\Delta_G$		$L_\theta$	
		Cat <sub>1</sub>	Cat <sub>2</sub>	Cat <sub>1</sub>	Cat <sub>2</sub>	Cat <sub>1</sub>	Cat <sub>2</sub>
$\mathcal{H}$	Cat <sub>1</sub>	0	0	0	1	0	0
	Cat <sub>2</sub>	0	0	1	0	0	0
$10^3\mathcal{K}$	Cat <sub>1</sub>	0	204	0	295	0	127
	Cat <sub>2</sub>	204	0	295	0	127	0

Table 5. Kolmogorov-Smirnov test for the discrimination of Cat<sub>1</sub> and Cat<sub>2</sub> based on features using interpolated periodogram in polar coordinates. Null hypothesis is rejected at the level  $\alpha = 0.05$  if  $\mathcal{K} > \mathcal{K}_s$  with  $\mathcal{K}_s \approx 1.36\sqrt{\frac{N_1+N_2}{N_1 \times N_2}}$ . With  $N_1 = 78$  (number of samples of Cat<sub>1</sub>) and  $N_2 = 88$  (number of samples of Cat<sub>2</sub>),  $\mathcal{K}_s \approx 0.212$ .

Stat	Cat <sub>k</sub> <sup>m</sup> \ Cat <sub>l</sub> <sup>n</sup>	G				$\Delta_G$				$L_\theta$			
		Cat <sub>1</sub> <sup>1</sup>	Cat <sub>1</sub> <sup>2</sup>	Cat <sub>2</sub> <sup>1</sup>	Cat <sub>2</sub> <sup>2</sup>	Cat <sub>1</sub> <sup>1</sup>	Cat <sub>1</sub> <sup>2</sup>	Cat <sub>2</sub> <sup>1</sup>	Cat <sub>2</sub> <sup>2</sup>	Cat <sub>1</sub> <sup>1</sup>	Cat <sub>1</sub> <sup>2</sup>	Cat <sub>2</sub> <sup>1</sup>	Cat <sub>2</sub> <sup>2</sup>
$\mathcal{H}$	Cat <sub>1</sub> <sup>1</sup>	0	0	0	0	0	0	1	1	0	0	1	1
	Cat <sub>1</sub> <sup>2</sup>	0	0	1	0	0	0	1	1	0	0	0	0
	Cat <sub>2</sub> <sup>1</sup>	0	1	0	0	1	1	0	0	1	0	0	0
	Cat <sub>2</sub> <sup>2</sup>	0	0	0	0	1	1	0	0	1	0	0	0
$10^3\mathcal{K}$	Cat <sub>1</sub> <sup>1</sup>	0	256	235	114	0	128	295	383	0	179	372	326
	Cat <sub>1</sub> <sup>2</sup>	256	0	366	265	128	0	306	374	179	0	206	195
	Cat <sub>2</sub> <sup>1</sup>	235	366	0	182	295	306	0	113	372	206	0	91
	Cat <sub>2</sub> <sup>2</sup>	113	265	182	0	383	374	113	0	326	195	91	0

Table 6. Kolmogorov-Smirnov test for the discrimination of sub-classes Cat<sub>1</sub><sup>m</sup> and Cat<sub>2</sub><sup>n</sup> of Cat<sub>1</sub> and Cat<sub>2</sub> respectively,  $m, n \in \{1, 2\}$ , based on features computed using PSD estimated with AR-based method in polar coordinates. Null hypothesis is rejected at the level  $\alpha = 0.05$  if  $\mathcal{K} > \mathcal{K}_s$  with  $\mathcal{K}_s \approx 1.36\sqrt{\frac{N_1+N_2}{N_1 \times N_2}}$ : for Cat<sub>1</sub><sup>1</sup> ( $N_1 = 39$ ) and Cat<sub>1</sub><sup>2</sup> ( $N_2 = 39$ ),  $\mathcal{K}_s \approx 0.308$ ; for Cat<sub>1</sub><sup>1</sup> ( $N_1 = 39$ ) and Cat<sub>2</sub><sup>1</sup> ( $N_2 = 44$ ),  $\mathcal{K}_s \approx 0.299$ ; for Cat<sub>1</sub><sup>1</sup> ( $N_1 = 39$ ) and Cat<sub>2</sub><sup>2</sup> ( $N_2 = 44$ ),  $\mathcal{K}_s \approx 0.299$ ; for Cat<sub>2</sub><sup>1</sup> ( $N_1 = 44$ ) and Cat<sub>2</sub><sup>2</sup> ( $N_2 = 44$ ),  $\mathcal{K}_s \approx 0.29$ .

evaluated by providing a comparison with a direct use of the PSD. Figure 7 provides the periodogram (proportional to the square of the modulus of the Discrete Fourier Transform, DFT) obtained by using zero-padding method for the same input image as in figure 4 - [third row]. This periodogram lacks smoothness and 2D Gaussian filters with standard deviations  $\sigma = 3, 6$  have been used for its regularization (see Fig.7, second and third rows).

The three proposed informative parameters are then computed from this periodogram in polar coordinates *via* spline interpolation (see Fig. 7). For the morphological analysis, different values of the threshold  $\lambda_1$  (see Eq. 15) are used: 0.6, 0.7, 0.8 and 0.9. The best discrimination results have been obtained for  $\sigma = 3$  and  $\lambda_1 = 0.8$ . For these values, statistics of the informative parameters (see Tab.3), kernel distributions (see Fig. 6 second row)

Stat	Cat <sub>k</sub> <sup>m</sup> \ Cat <sub>l</sub> <sup>n</sup>	G				$\Delta_G$				$L_\theta$			
		Cat <sub>1</sub> <sup>1</sup>	Cat <sub>1</sub> <sup>2</sup>	Cat <sub>2</sub> <sup>1</sup>	Cat <sub>2</sub> <sup>2</sup>	Cat <sub>1</sub> <sup>1</sup>	Cat <sub>1</sub> <sup>2</sup>	Cat <sub>2</sub> <sup>1</sup>	Cat <sub>2</sub> <sup>2</sup>	Cat <sub>1</sub> <sup>1</sup>	Cat <sub>1</sub> <sup>2</sup>	Cat <sub>2</sub> <sup>1</sup>	Cat <sub>2</sub> <sup>2</sup>
$\mathcal{H}$	Cat <sub>1</sub> <sup>1</sup>	0	0	0	0	0	0	0	1	0	1	0	0
	Cat <sub>1</sub> <sup>2</sup>	0	0	0	1	0	0	1	1	1	0	0	1
	Cat <sub>2</sub> <sup>1</sup>	0	0	0	0	0	1	0	1	0	0	0	0
	Cat <sub>2</sub> <sup>2</sup>	0	1	0	0	1	1	1	0	0	1	0	0
$10^3\mathcal{K}$	Cat <sub>1</sub> <sup>1</sup>	0	197	185	218	0	286	187	402	0	322	167	105
	Cat <sub>1</sub> <sup>2</sup>	197	0	199	300	286	0	314	458	322	0	224	342
	Cat <sub>2</sub> <sup>1</sup>	185	199	0	126	187	314	0	300	167	224	0	118
	Cat <sub>2</sub> <sup>2</sup>	218	300	126	0	402	458	300	0	105	342	118	0

Table 7. Kolmogorov-Smirnov test for the discrimination of sub-classes Cat<sub>1</sub><sup>m</sup> and Cat<sub>2</sub><sup>n</sup> of Cat<sub>1</sub> and Cat<sub>2</sub> respectively,  $m, n \in \{1, 2\}$ , based on features computed using interpolated periodogram in polar coordinates. Null hypothesis is rejected at the level  $\alpha = 0.05$  if  $\mathcal{K} > \mathcal{K}_s$  with  $\mathcal{K}_s \approx 1.36 \sqrt{\frac{N_1 + N_2}{N_1 \times N_2}}$ : for Cat<sub>1</sub><sup>1</sup> ( $N_1 = 39$ ) and Cat<sub>1</sub><sup>2</sup> ( $N_2 = 39$ ),  $\mathcal{K}_s \approx 0.308$ ; for Cat<sub>1</sub><sup>1</sup> ( $N_1 = 39$ ) and Cat<sub>2</sub><sup>1</sup> ( $N_2 = 44$ ),  $\mathcal{K}_s \approx 0.299$ ; for Cat<sub>1</sub><sup>1</sup> ( $N_1 = 39$ ) and Cat<sub>2</sub><sup>2</sup> ( $N_2 = 44$ ),  $\mathcal{K}_s \approx 0.299$ ; for Cat<sub>2</sub><sup>1</sup> ( $N_1 = 44$ ) and Cat<sub>2</sub><sup>2</sup> ( $N_2 = 44$ ),  $\mathcal{K}_s \approx 0.29$ .

and Kolmogorov-Smirnov tests (see Tab.5 & 7) are performed.

The main conclusion remains the same (the two catalysts can be discriminated) but only with the distribution of the distance variation: the tangential length is no longer discriminant with the direct approach whereas the results obtained for some sub-populations show discriminations between catalysts for both the distance variation and the tangential length (see Tab.7).

HRTEM observations of the two catalysts show important differences in the organization of the active phase on the support: Cat1, containing high amounts of active phase, presents as well stacks and aggregates of CoMoS slabs, in which slabs appear curved whereas Cat 2 presents isolated slabs of stacks of slabs, with a rather straight morphology. This difference is not clearly expressed by traditional measures of the length and stacking numbers.  $L_\theta$  is higher in Cat 1 (the CoMoS/alumina catalyst with high Mo loading) as it can be observed in Tab.2 and Fig.6, first row. It is in coherence with the observation of aggregated slabs.  $L_\theta$  translates the curvature of the slabs and can be a proper descriptor of the aggregation of the slabs. The discrimination of the catalysts using the distribution of  $L_\theta$  is obtained using AR-based method for PSD estimation and not the Fourier-based method (see Tab.4 & 5).

Thus, ARFBF morphology characterization proposed in the paper seems to be a promising feature-based description to separate the two sets of HRTEM images representing active phases of the two catalysts.

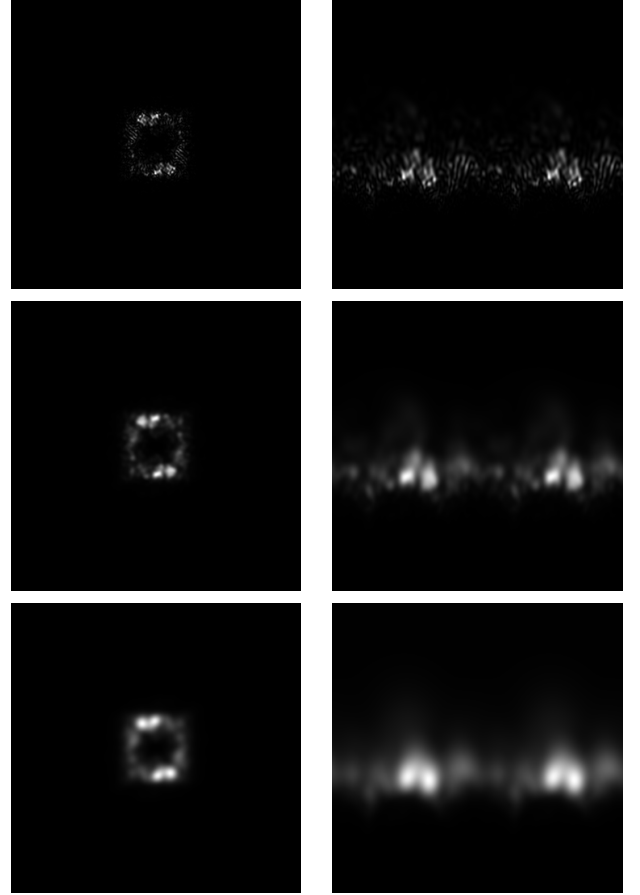


Figure 7. PSD estimated using the square of the modulus of the Discrete Fourier Transform. 1st row: left, periodogram with size  $512 \times 512$  obtained using zero-padding method (PSD1); right, interpolated PSD1 in polar coordinates. 2nd row: left, PSD1 smoothed by a Gaussian filter with  $\sigma = 3$  (PSD2); right, interpolated

*PSD2 in polar coordinates. 3rd row: left, PSD1 smoothed by a Gaussian filter with  $\sigma = 6$  (PSD3); right, interpolated PSD3 in polar coordinates.*

## CONCLUSION

In this paper, we have proposed an ARFBF based morphological description of HRTEM image morphological textures corresponding to the observation of material micro-structures at nanometer scale. This morphological description is based on 2-D parametric spectrum estimation.

We described the different components of the ARFBF model and we explained parameter estimation methods that lead to 2-D spectrum estimation. For the estimation of FBF Hurst parameter, we made a comparative study of different methods in order to select a robust one with respect to different sampling generators.

The obtained Hurst and AR features provide a description of heterogeneous HRTEM image as a stochastic field, where the active phase fringes are associated with AR parameters and geometric fringe features have been derived by morphology analysis of the spectral fringe information.

The analysis proposed allows to discriminate between two catalyst classes and opens some prospects on automatic monitoring of active phases associated with different materials, as well as material at nanoscale.

It would be interesting to investigate further, the relationship between the catalytic performance and the value of  $L_\theta$  parameter.

## ACKNOWLEDGMENT

This research was supported by ARC6 grant from Rhône-Alpes French region. The authors would like to thank the reviewers (their feedback has allows a significant improvement of the paper quality) and also Anne Sophie Gay from IFPEN for her valuable help.

## LIST OF SYMBOLS

- A: 2-D Auto-Regressive (AR) field.
- $QP_l$ : prediction domains for A and associated with quarter plans,  $l = 1, 2$ .

- $D \subset \mathbb{Z}^2$ : prediction support for A. For instance,
  - $D_{QP_1} = \{0 \leq m_1 \leq M_1, 0 \leq m_2 \leq M_2\} \setminus (0, 0)$ ;
  - $D_{QP_2} = \{-M_1 \leq m_1 \leq 0, 0 \leq m_2 \leq M_2\} \setminus (0, 0)$ .
- $(M_1, M_2)$ : order of the 2-D AR model ( $M_1 = M_2 = 10$  are used for experimental results).
- $\theta_{M_1, M_2}^{QP_l}$  set of parameters with the form  $\{\sigma_{e,l}^2, \{\beta_{m,l}, m \in D_{QP_l}\}\}$  of the AR model.
- $B_H$ : isotropic fractional Brownian field with Hurst parameter H,  $0 < H < 1$ .
- $R_H$ : auto-correlation function of  $B_H$ .
- Z: ARFBF, spatial deterministic convolution of field A and field  $B_H$ .
- S: power spectral density (PSD).
- $\hat{S}_B(u, v)$ : wavelet packet spectrum in Cartesian coordinates  $(u, v)$ .
- $S_p(r, \theta)$ : PSD in polar coordinate.
- $S^*(r, \theta)$ : PSD calculated from AR estimated parameters in polar coordinate.
- $S_1^*(r, \theta)$ : PSD after remove the contribution of the first lobe on  $S^*$ .
- $P_1, P_2$ : frequencies providing maximum values of  $S^*, S_1^*$  respectively.
- $\alpha_1, \alpha_2$ : thresholds for  $S^*, S_1^*$  respectively.
- $\lambda_1 \in [0, 1], \lambda_2 \in [0, \lambda_1]$ :  $\alpha_1 = \lambda_1 S^*(P_1)$  and  $\alpha_2 = \lambda_2 S^*(P_1)$ .
- $S^{**}, S_1^{**}$ : binary images from  $S^*, S_1^*$  when using thresholds  $\alpha_1, \alpha_2$ , respectively.
- $Q_1, Q_2$ : binary images obtained by using morphological reconstructions with markers  $P_1, P_2$ , respectively.
- R: radius of disk in morphological dilation.
- $T_e$ : sampling period.
- G: distance value.
- $\Delta_G$ : distance variation (regularity of spacing).
- $L_\theta$ : tangential length (regularity of curvature).
- $\Gamma$ : standard gamma special function.
- T: Cartesian-to-polar transform.

## REFERENCES

- Akaike, H.  
(1974). A new look at the statistical model identification. *IEEE Transactions on Automatic Control*, 19(6):716 – 723.
- Alata, O. and C. Cariou  
(2008a). *Two-Dimensional Signal Analysis, Chapter "2-D Linear Stochastic Modeling"*, chapter 2, Pp. 65–114. ISTE, Wiley.
- Alata, O. and C. Cariou  
(2008b). *Two-Dimensional Signal Analysis, Chapter "2-D Spectral Analysis"*, chapter 3, Pp. 115–174. ISTE, Wiley.
- Alata, O., C. Cariou, C. Ramananjara, and M. Najim  
(1998). Classification of rotated and scaled textures using HMHV spectrum estimation and the Fourier-Mellin transform. In *IEEE Int. Conf. Image Processing, ICIP*, volume 1, Pp. 53–56.
- Alata, O. and C. Olivier  
(2003). Choice of a 2-D causal autoregressive texture model using information criteria. *Pattern Recognition Letters*.
- Alata, O. and C. Ramananjara  
(2005). Unsupervised textured image segmentation using 2-D quarter plane autoregressive support with four prediction support. *Pattern Recognition Letters*, 26:1069–1081.
- Atto, A., Y. Berthoumieu, and P. Bolon  
(2013). 2-dimensional wavelet packet spectrum for texture analysis. *IEEE Transactions on Image Processing*, 22(6):2495–2500.
- Atto, A., D. Pastor, and G. Mercier  
(2010). Wavelet packets of fractional brownian motion: Asymptotic analysis and spectrum estimation. *IEEE Transactions on Information Theory*, 56:4741 – 4753.
- Atto, A., Z. Tan, O. Alata, and M. Moreaud  
(2014). Non-stationary texture synthesis from random field modeling. In *IEEE Int. Conf. Image Processing, ICIP*, Pp. 4266–4270.
- Celce, B., S. Bres, F. Moreau, P. Gueroult, and L. Sorbier  
(2008). Semi-automatic detection of sulfur slabs. *STERMAT 2008 : VIII International Conference on Stereology and Image Analysis in Materials Sciences, 2–6 septembre 2008 Zakopane, Polska. Inzynieria Materiałowa 29 (4) : 421–426*.
- Da Costa, J.-P., P. Weisbecker, B. Farbos, J. Leyssale, G. Vignoles, and C. Germain  
(2015). Investigating carbon materials nanostructure using image orientation statistics. *Carbon*, 84:160–173.
- Fieguth, P. W. and A. S. Willsky  
(1996). Fractal estimation using models on multiscale trees. *IEEE Trans. Signal Proc.*, 44:1297–1300.
- Geantet, C. and L. Sorbier  
(2012). Chapter 2.6 - Characterisation of catalysts. *STDI Frame Maker*.
- Geweke, J. and S. Porter-Hudak  
(1983). The estimation and application of long memory time series models. *Journal of Time Series Anal.*, 4:221–237.
- Goncalves, W. and O. Bruno  
(2013). Combining fractal and deterministic walkers for texture analysis and classification. *Pattern Recognition*, 46:2953–2968.
- Haralick, R. M.  
(1979). Statistical and structural approaches to texture. *Proceedings of the IEEE*, 67(5):786 – 804.
- Huang, Q., J. R. Lorch, and R. C. Dubes  
(1994). Can the fractal dimension of images be measured? *Pattern Recognition*, 27(3):339–349.
- Huang, Z. and C. Li  
(2005). Anisotropic fractional brownian random fields as white noise functionals. *Acta Mathematicae Applicatae Sinica, English Series*, 21(4):655–660.
- Jackson, L. B. and H. C. Chien  
(1979). Frequency and bearing estimation by two-dimensional linear prediction. In *IEEE Int. Conf. Acoustic Speech and Sig. Proc., ICASSP*, Pp. 665 – 668.
- Kroese, D. P. and Z. I. Botev  
(2013). Spatial process generation. *Statistics Computation*.
- Mandelbrot, B. B. and J. W. V. Ness  
(1968). Fractional Brownian motions, fractional noises and application. *SIAM Review*, 10(4):422–437.
- Mao, J. and A. Jain  
(1992). Texture classification and segmentation using multi-resolution simultaneous autoregressive (MR-SAR) models. *Pattern Recognition*, 25(2):173–188.
- Moreaud, M., D. Jeulin, V. Morard, and R. Revel  
(2012). TEM image analysis and modelling:

- application to boehmites nanoparticles. *Journal of Microscopy*, 245(2):186–199.
- Moreaud, M., D. Jeulin, A. Thorel, and J. Y. Chane-Ching (2008). A quantitative morphological analysis of nanostructured ceria-silica composite catalysts. *Journal of Microscopy*, 232:293–305.
- Nason, G. and B. Silverman (1995). The stationary wavelet transform and some statistical applications. *Lecture Notes in Statistics*, 103:281–299.
- Nikulshin, P., D. Ishutenko, A. Mozhaev, K. Maslakov, and A. Pimerzin (2014). Effects of composition and morphology of active phase of CoMo/Al<sub>2</sub>O<sub>3</sub> catalysts prepared using Co<sub>2</sub>Mo<sub>10</sub>-heteropolyacid and chelating agents on their catalytic properties in HDS and HYD reactions. *Journal of Catalysis*, 312:152–169.
- Parzen, E. (1962). On estimation of a probability density function and mode. *Ann. Math. Statist.*, 33:1065–1076.
- Peacock, J. (1983). Two-dimensional goodness-of-fit testing in astronomy. *Monthly Notices of the Royal Astronomical Society*, 202(3):615–627.
- Pesquet-Popescu, B. and P. Larzabal (1997). 2D self-similar processes with stationary fractional increments. *Springer-Verlag in Fractals in Engineering*, Pp. 138–151.
- Pesquet-Popescu, B. and J. L. Véhel (2002). Stochastic fractal models for image processing. *IEEE Signal Processing Magazine*, 19:48–62.
- Pré, P., G. Huchet, D. Jeulin, J. Rouzaud, M. Sennour, and A. Thorel (2013). A new approach to characterize the nanostructure of activated carbons from mathematical morphology applied to high resolution transmission electron microscopy images. *Carbon* 52, Pp. 239–258.
- Qazi, I.-U.-H., O. Alata, J.-C. Burie, A. Moussa, and C. Fernandez-Maloigne (2011). Choice of a pertinent color space for color texture characterization using parametric spectral analysis. *Pattern Recognition Letters*, 44:16–31.
- Ranganath, S. and A. K. Jain (1985). Two-dimensional linear prediction models - part I: spectral factorization and realization. *IEEE Trans. on Acoustic Speech and Signal Processing*, ASSP-33(1):280–299.
- Richard, F. and H. Bierme (2010). Statistical tests of anisotropy for fractional Brownian textures. Application to full-field digital mammography. *Journal of Mathematical Imaging and Vision*, 36(3):227 – 240.
- Robinson, P. M. (1995). Log-periodogram regression of times series with long range dependence. *The Annals of Statistics*, 23(3):1048–1072.
- Rosenblatt, M. (1956). Remarks on some nonparametric estimates of a density function. *Ann. Math. Statist.*, 27:832–837.
- Serra, J. (1988). Image analysis and mathematical morphology: Theoretical advances. *Academic Press, London*.
- Souza, P. (1982). Texture recognition via autoregression. *Pattern Recognition*, 15(6):471–475.
- Tafti, P., D. Van De Ville, and M. Unser (2009). Invariances, Laplacian-like wavelet bases, and the whitening of fractal processes. *IEEE Trans. on Image Processing*, 18:689 – 702.
- Tan, Z., A. Atto, O. Alata, and M. Moreaud (2015). ARFBF model for non-stationary random fields and application in HRTEM images. In *IEEE Int. Conf. on Image Processing, ICIP*.
- Toth, P., A. Palotas, E. Eddings, R. Whitaker, and J. Lighty (2013). A novel framework for the quantitative analysis of high resolution transmission electron micrographs of soot II. Robust multiscale nanostructure quantification. *Combustion and Flame*, 160:920–932.
- Toulhoat, H. and P. Raybaud (2013). Catalysis by transition metal sulphides - from molecular theory to industrial application. *IFP Publications*.
- Van De Ville, D., T. Blu, and M. Unser (2005). Isotropic polyharmonic B-splines: Scaling functions and wavelets. *IEEE Trans. on Image Processing*, 14:1798 – 1813.
- Yehliu, K., R. V. Wal, and A. Boehman (2011). Development of an HRTEM image analysis method to quantify carbon nanostructure. *Combustion and Flame*, 158:1837–1851.



Zhang, B. S., Y. J. Yi, W. Zhang, C. H. Liang, and  
D. S. Su  
(2011). Electron microscopy investigation of

the microstructure of unsupported Ni-Mo-W  
sulfide. *Materials Characterization*, 62:684-  
690.